

Three-dimensional ray-tracing model for the study of advanced refractive errors in keratoconus

STAFFAN SCHEDIN,^{1,*} PER HALLBERG,¹ AND ANDERS BEHNDIG²

¹Department of Applied Physics and Electronics, Umeå University, SE-90187 Umeå, Sweden

²Department of Clinical Sciences/Ophthalmology, Umeå University, SE-90187 Umeå, Sweden

*Corresponding author: Staffan.Schedin@umu.se

Received 27 August 2015; revised 7 December 2015; accepted 7 December 2015; posted 7 December 2015 (Doc. ID 248420); published 14 January 2016

We propose a numerical three-dimensional (3D) ray-tracing model for the analysis of advanced corneal refractive errors. The 3D modeling was based on measured corneal elevation data by means of Scheimpflug photography. A mathematical description of the measured corneal surfaces from a keratoconus (KC) patient was used for the 3D ray tracing, based on Snell's law of refraction. A model of a commercial intraocular lens (IOL) was included in the analysis. By modifying the posterior IOL surface, it was shown that the imaging quality could be significantly improved. The RMS values were reduced by approximately 50% close to the retina, both for on- and off-axis geometries. The 3D ray-tracing model can constitute a basis for simulation of customized IOLs that are able to correct the advanced, irregular refractive errors in KC. © 2016 Optical Society of America

OCIS codes: (170.4460) Ophthalmic optics and devices; (220.2740) Geometric optical design; (330.1070) Vision - acuity; (330.7326) Visual optics, modeling; (330.7333) Visual optics, refractive anomalies.

<http://dx.doi.org/10.1364/AO.55.000507>

1. INTRODUCTION

Keratoconus (KC) is a noninflammatory progressive corneal degeneration in which the cornea becomes thinner and eventually protrudes and assumes a cone-like shape. The corneal protrusion causes irregular astigmatism, affecting visual quality [1]. Ocular symptoms vary depending on the disease severity. In early stages of the disease, the refractive errors can be corrected with glasses or rigid contact lenses, but in late stages when the disease becomes more severe, glasses are not sufficient to achieve acceptable visual quality and keratoplasty may be the only option left [2]. None of these interventions, however, have any effect on the underlying causes of the disease.

Today corneal collagen cross linking (CXL) has emerged as an established treatment for progressive KC. CXL combines riboflavin and ultraviolet light to increase the biomechanical stability of the cornea and halt disease progression [3]. Thus, many patients suffering from KC today have stabilized, albeit irregular, refractive errors that require advanced rigid contact lens solutions to achieve acceptable visual quality.

Today, replacement of the crystalline lens with an artificial intraocular lens (IOL) is a standard procedure, whether done as a cataract procedure or as a refractive lens exchange (RLE). With modern biometry methods and surgical techniques, the results after such procedures have become highly predictable [4],

the visual rehabilitation is quick [5], and the complication frequencies are low [6].

A corneal transplantation, on the other hand, often results in substantial refractive errors after a long healing process, and also carries rather high risk of serious complications such as graft rejection [7]. Compared to a corneal transplantation, replacement of the crystalline lens by a custom-made IOL with the ability to compensate for the advanced refractive errors of KC could prove an attractive alternative if the disease is first stabilized by CXL. Construction of such an IOL could be based on three-dimensional (3D) ray tracing, a method used previously to estimate refractive power, then often by using commercial systems [8–11]. Ray tracing in combination with topographic measurements of the anterior corneal surface have previously been used for analysis of personalized IOLs. For example, Rosales and Marcos [12] used ray tracing to simulate aberrations on customized computer eye models, where individual measurements of corneal topography were used. Einigamhamer *et al.* [13,14] developed a real ray-tracing model to calculate the geometry of custom IOLs for cataract surgery. A theoretical biconic surface was used to model the toricity and asphericity of the IOL [13].

In this paper, we address an approach to analyze the advanced refractive errors in diseases like KC, using numerical

methods based on 3D ray tracing and measured corneal data by means of Scheimpflug photography. Elevation data of both the anterior and posterior corneal surfaces are used in the ray-tracing analysis. In addition, with the ray-tracing model as a basis, we present an approach to modify the posterior surface of a spherical IOL to a free-form shape to compensate for any type of advanced refractive error.

2. 3D RAY-TRACING METHOD

Consider a light ray in 3D space that intersects and refracts at a surface between two different transparent media (Fig. 1). To calculate the direction T of the refracted ray, we need the direction cosines of the incoming ray vector, $I = (I_x, I_y, I_z)$, and those of the normal vector to the surface, $N = (N_x, N_y, N_z)$, at the intersection point. We also need the spatial location of the point where the ray intersects with the surface, which is defined by the surface coordinate (x, y, z) . If the surface can be described by an analytical function, e.g., a second-degree function like a sphere, the intersection coordinates and the normal vectors at each intersection point can be determined algebraically. However, this is not the case when dealing with measurement data, as in this study, that represent surfaces deviating from ideal mathematical ones. Therefore, an appropriate numerical method is needed. Earlier works that address the problem of finding the intersection points of rays with optical surfaces are found in the literature [15–17]. For examples, Ortiz *et al.* [17] developed a method based on Delaunay triangulation of ray tracing, in which the surface is approximated with a set of flat triangles.

In this work, the measurement data originated from a smooth but slightly deformed topography of the cornea, using the Scheimpflug camera. A fitting procedure of the measured data to a second-degree polynomial approximation of a set of surface elements was implemented to determine the intersection points and their normal vectors. Unlike, e.g., Zernike polynomials, which model the global shape of an optical surface, we model the local variation of the shape. The surface was divided into a number of elements, each defined by nine neighboring grid points, to obtain the data needed for the ray-tracing procedure.

Let $P_i = (x_i, y_i, z_i)$ represent the measured grid points that constitutes the surface, $i = 1, 2, \dots, n$, where n is the total number of points. The measured points are regularly spaced in the x and y directions, which means that they can be visualized as a regular grid in 3D space, as shown in Fig. 1. Moreover, consider an incoming ray that emanates from a coordinate $P_0 = (x_0, y_0, z_0)$ with a normalized direction vector $I = (I_x, I_y, I_z)$.

First, a set of distance vectors, $d_i = (d_{xi}, d_{yi}, d_{zi})$ is computed from every grid point on the surface, P_i , to the coordinate P_0 , i.e., $d_i = P_i - P_0$. Next, the grid point, $P_c = (x_c, y_c, z_c)$, that is closest to the location where the incoming ray will hit the surface is determined. This is done by finding the minimum difference between each of the distance vectors from the set $d_i (i = 1, 2, \dots, n)$ and the incoming ray vector, i.e., P_c is found by evaluating the condition $\min |d_i - I|$, $i = 1, 2, \dots, n$. The grid point P_c and its eight neighboring points form a surface element, which is fitted to a second-degree polynomial of the form

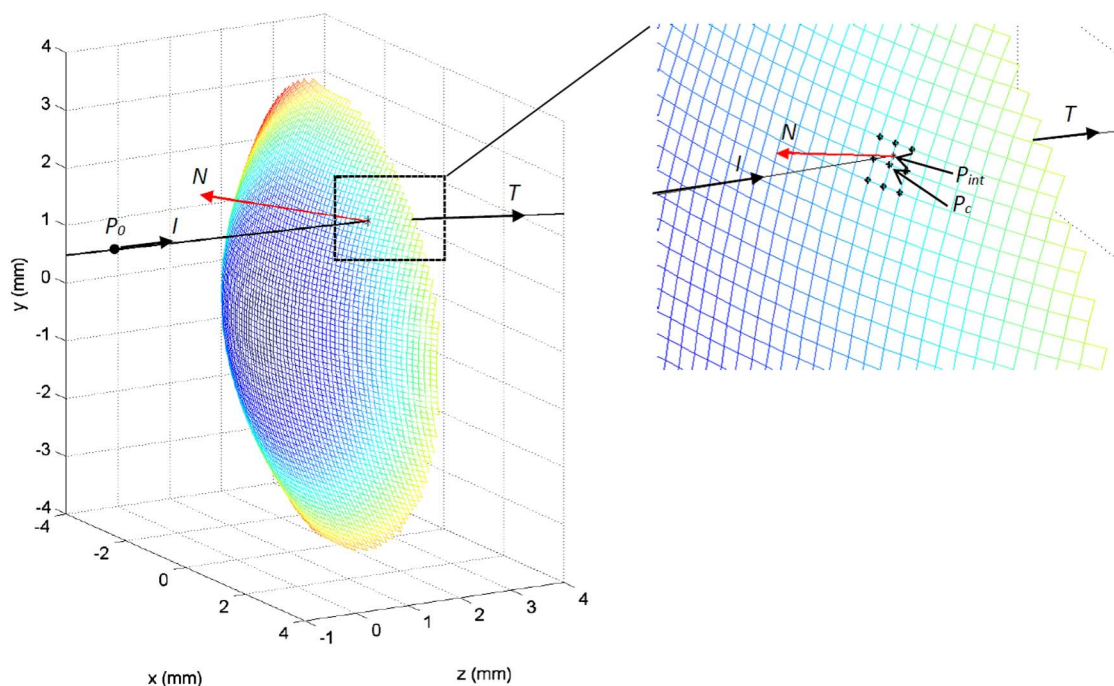


Fig. 1. Principle of the 3D ray-tracing model. A light ray traveling in 3D space intersects and refracts at a corneal surface constructed from measurement data. The direction of the refracted ray, $T = (T_x, T_y, T_z)$, is calculated by means of a 3D version of Snell's law. The direction cosines of the incoming ray vector are $I = (I_x, I_y, I_z)$, and those of the normal vector $N = (N_x, N_y, N_z)$ at the intersection point. P_c is the measured grid point closest to the location where a ray that emanates from point P_0 hits the surface. The coordinates of the intersection point, P_{int} , are found by fitting a surface element, formed by nine neighboring grid points, to a second-degree polynomial.

$$z = f(x, y) = A + Bx + Cy + Dx^2 + Exy + Fy^2. \quad (1)$$

MATLAB (curve fitting toolbox) was used for numerical evaluation of the coefficients A, B, \dots, F and accuracy of the fit. The incoming ray constitutes a straight line described in parametric form by

$$\begin{cases} x = x_0 + I_x t \\ y = y_0 + I_y t \\ z = z_0 + I_z t \end{cases} \quad (2)$$

where t is the linear parameter. The intersection coordinates $P_{\text{int}} = (x_{\text{int}}, y_{\text{int}}, z_{\text{int}})$ are calculated by substituting Eq. (2) into Eq. (1) and solving for t . After the intersection point has been determined, the components of the normal vector at this point were assessed by means of the partial derivatives of Eq. (1):

$$\begin{cases} N_x(x, y) = \frac{\partial f(x, y)}{\partial x} \\ N_y(x, y) = \frac{\partial f(x, y)}{\partial y} \\ N_z(x, y) = -1 \end{cases} \quad (3)$$

The procedure of finding the intersection point and the normal vector was repeated for the total number of rays that were included in the analysis. The number of rays analyzed could be chosen arbitrarily. The data for all rays (the normalized Cartesian components of \mathbf{I} , \mathbf{N} and the intersection coordinates) were handled by two-dimensional matrices in MATLAB. Next, the directions, $\mathbf{T} = (T_x, T_y, T_z)$, of the refracted rays were calculated by means of a 3D version of Snell's law [18]:

$$\mathbf{T} = \eta \mathbf{I} + [\eta(\mathbf{N} \cdot \mathbf{I}) - \sqrt{1 - \eta^2 + \eta^2(\mathbf{N} \cdot \mathbf{I})^2}] \mathbf{N}, \quad (4)$$

where η is the refractive index of medium 2 relative to medium 1, i.e., $\eta = \eta_2/\eta_1$. The dot product between \mathbf{N} and \mathbf{I} is denoted by $\mathbf{N} \cdot \mathbf{I}$. Equation (4) is conveniently applied to the matrices that contain the components of all rays, i.e., the refracted direction for each component was obtained for all the rays at the same time in a single matrix multiplication. An additional step needed throughout the calculations was the normalization of the vectors \mathbf{I} , \mathbf{N} , and \mathbf{T} , i.e., the magnitude of these vectors should be unitary. This was done by scaling by the reciprocal of their magnitudes. For example, the normalized components of the refracted ray vector (\hat{T}_x , \hat{T}_y , and \hat{T}_z) were obtained according to

$$\begin{cases} \hat{T}_x = T_x/|\mathbf{T}| \\ \hat{T}_y = T_y/|\mathbf{T}| \\ \hat{T}_z = T_z/|\mathbf{T}| \end{cases} \quad (5)$$

where $|\mathbf{T}| = \sqrt{T_x^2 + T_y^2 + T_z^2}$ is the magnitude (length) of \mathbf{T} . Analogous expressions were applied for normalization of vectors \mathbf{N} and \mathbf{I} . The ray-tracing procedure continues with the second surface in the system, and the calculation steps described above are repeated.

Finally, an IOL was introduced in the model, so the ray-tracing procedure could be completed through the entire optical system of the eye and the focusing ability, in terms of spot diagrams, could be analyzed. The surfaces of the IOL were modeled as a quadric function (equation of a sphere). In this case, the division of the surface into a number of elements and

the fitting procedure were not needed since the points and normal vectors could be found algebraically. In principle, any number of surfaces, both based on analytical and measured data, can be included in this ray-tracing procedure.

The results of the ray tracing were evaluated in terms of spot diagrams at the x and y planes corresponding to the position of the retina showing the spread of the bundle of rays. The spot diagrams represent the coordinates of the intersection of the calculated rays with selected x - y planes in the focal region. For each plane, the centroid of the distribution of rays, x_{ct} and y_{ct} , as well as the RMS values, r_{rms} , of the spot radius were obtained by means of the following expressions [19]:

$$x_{ct} = \frac{1}{N} \sum_{i=1}^N x_i \quad (6)$$

$$y_{ct} = \frac{1}{N} \sum_{i=1}^N y_i \quad (7)$$

$$r_{\text{rms}} = \sqrt{\frac{1}{N} \sum_{i=1}^N [(x_i - x_{ct})^2 + (y_i - y_{ct})^2]}, \quad (8)$$

where x_i and y_i are the x and y coordinates, respectively, of the rays that intersect with the planes. N is the total number of rays.

3. CORNEAL DATA OBTAINED WITH SCHEIMPFLUG PHOTOGRAPHY

An example of the elevation data of the anterior and the posterior cornea surfaces from a patient with advanced KC was obtained with Scheimpflug photography (Pentacam HR, Oculus, Inc., Lynnwood, Washington). The study was approved by the Regional Ethical Review Board of Umeå University, Umeå, Sweden, and was performed in accordance with the Declaration of Helsinki. The output elevation data is arranged in a number of discrete measurement points in space, each point defined by an x , y , and z coordinate. In our example, the x and y coordinates form a grid of total size 14 mm \times 14 mm, with equal spacing of 0.1 mm between each pair of points, giving a total number of points of 19,600. The vertex of the anterior surface is positioned at the origin of the co-ordinate system, ($x = y = z = 0$). Elevation data are normally presented as a topography map in relation to a spherical reference body. Figures 2(a) and 2(b) demonstrate the elevation maps in our example for the anterior and the posterior corneal surfaces, respectively. The elevation maps clearly show the typical ring shape due to a deformed surface as a result of KC. The radii of curvature of the reference sphere were found by fitting the elevation data to spherical surfaces in the least square sense [20]. In that way, the radii of the best fitting spheres for the anterior and the posterior surface were determined to be 7.48 mm and 6.22 mm, respectively.

The Pentacam measurement data of the anterior and the posterior surfaces of the cornea provide the basic input to our eye ray-tracing model. Moreover, for the other ophthalmic elements, we used the input parameters listed in Table 1, obtained from literature.

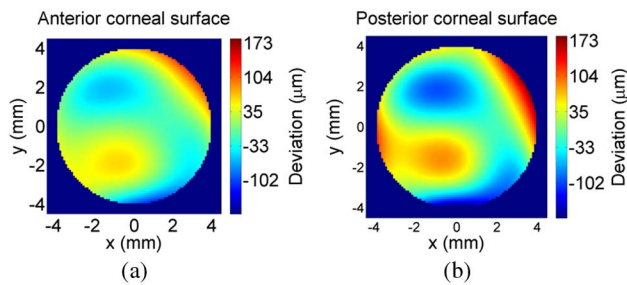


Fig. 2. Elevation maps showing the shape of the example cornea surfaces degraded by KC. (a) The anterior corneal surface relative to a spherical body with radius 7.48 mm and (b) the posterior corneal surface relative to a sphere with radius 6.22 mm.

The IOL was modeled mathematically by means of two opposite convex spherical surfaces, separated by a distance of 0.633 mm (based on SN60WF, Acrosf lenses by Alcon) [22]. These surfaces are described by the general equation of a sphere:

$$(z - z_c)^2 = R^2 - (x - x_c)^2 - (y - y_c)^2, \quad (9)$$

where R is the radius, and (x_c, y_c, z_c) represent the distances from the center of the sphere to the cornea vertex, i.e., to the origin of the coordinate system. The IOL is positioned symmetrically around the z axis; that is, $x_c = y_c = 0$. Furthermore, the normal vector components are obtained by Eq. (3) and the intersection coordinates by substituting Eq. (2) into Eq. (9) and solving for the linear parameter t .

Apertures with specified diameters can conveniently be introduced in the ray-tracing model. In the present analysis, we use circular apertures of diameters of 6 and 3 mm, corresponding to normal pupil diameters at bright and dark conditions, respectively. A diameter of 3 mm was chosen to simulate vision under mesopic light conditions. The number of traced rays in this concept study is chosen to be one ray per measured grid point in the lateral directions. With grid-point spacing of 0.1 mm, this results in 5026 rays with aperture size of 6 mm, and 1256 rays with aperture size of 3 mm.

4. RESULTS

A. On-Axis System

Figures 3(a) and 3(b) demonstrate visualizations of the ray tracing through the entire optical system. The incoming rays originate from an on-axis point source located at infinity $P_0 = (0, 0, -100, 000)$ mm (parallel rays). The two convex surfaces to the left represent the measured anterior and posterior cornea, whereas the IOL is represented by the surfaces to the right.

Goodness of fits were evaluated, and it was found that the averages of the R-square value were 0.9998 and 0.9999 for the first and second surfaces, respectively. Thus, the variation of the elevation data is very well reproduced by the fits.

The imaging quality is further analyzed by means of the spot diagrams shown in Figs. 4(a) and 4(b). The relatively large spread of rays is an indication of severe aberrations due to KC. Table 2 shows a summary of the spot diagram analysis. The minimum spot radius (minimum of r_{rms}) was found to be located at $z = 21.77$ mm, for a pupil (aperture) diameter of 6 mm. Figure 3(b) displays the traced rays through the entire optical system as a result of the second analysis with a pupil diameter of 3 mm. By inspecting the fan of rays, we can already conclude a more narrow and distinct region around the focus. The spot diagrams in Fig. 4(b) show that the distribution of rays is found within a much smaller area compared with the case of a pupil diameter of 6 mm.

The smaller is the pupil diameter of the optical system, the more it approaches paraxial imaging conditions. The smaller extent of the spot is a result of a smaller region of peripheral rays traveling through the system, which, in turn, results in less transverse spherical aberration. Also, the minimum spot radius is found at a slightly larger distance, at $z = 21.79$ mm, in the case of the smaller pupil. That is, the smaller is the pupil, the less is the longitudinal spherical aberration [24]. Moreover, to relate the results to commonly used image quality metrics, we estimated the Strehl ratio of the system. The Strehl ratio is defined as the peak intensity of the point spread function (PSF), divided by the peak intensity of the PSF in the absence of aberration [25]. Here, we evaluated the PSF geometrically by means of sampling the rays at a regular grid with equally sized bins on the image plane. This resulted in a spatial distribution of the ray intensity that constituted a quantitative measure of the PSF. The peak intensity of the PSF in the absence of aberration was calculated from the “perfect” image point produced by the modified IOL. As expected, the Strehl ratio of the aberrated system depends strongly on the pupil diameter (Table 2).

In an approach to compensate for the image aberrations that result from the deformed corneal surfaces, we use the ray-tracing model to modify the posterior surface of the IOL in a way that it produces a “perfect” image of the point source. This is a kind of inverse problem, to find a custom-made IOL that corrects for the imaging errors, given a specified focal point. Altering a lens surface involves several degrees of freedom and can be realized in several ways, by, for example, changing the lens surface geometry or its index of refraction. In this concept study, we alternate the normal vectors of the posterior lens surface at the ray–surface intersection points in order to redirect

Table 1. Input Parameters for the Ray-Tracing Procedure

Ocular Element	Refractive Index	Radius of Curvature (mm)	Distance from Cornea Vertex (mm)
Cornea anterior	1.3771 [21]	elevation data, Pentacam	0.0
Cornea posterior	1.3771 [21]	elevation data, Pentacam	elevation data, Pentacam
Anterior chamber	1.3374 [21]	—	—
IOL anterior	1.554 [22]	19.6 [22]	3.6 [23]
IOL posterior	1.554 [22]	−20.0 [22]	4.2 [22]
Vitreous chamber	1.336 [21]	—	—

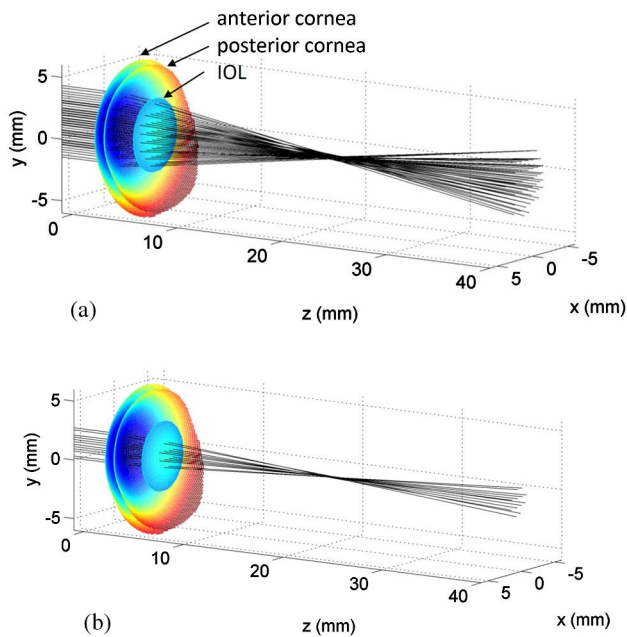


Fig. 3. Ray tracing through the schematic eye optical system with parallel incoming rays (point source located on axis at infinity). x , y , and z are the physical distances (mm). The first two surfaces at the left-hand side represent the cornea (from the Pentacam measurement data). The second and third surfaces represent a simulated spherical IOL with parameters taken from the literature. The system suffers from refractive errors as a result of the uneven cornea surfaces due to KC. (a) Pupil diameter (aperture) 6 mm. (b) Pupil diameter 3 mm. For visualization purposes, only a small fraction (1/64) of the total number of the rays are displayed in the figures.

the refracted rays toward a distinct focal point. First, the distance vectors, $d_i = (d_{xi}, d_{yi}, d_{zi})$, from the intersection points on the posterior lens surface to the specified focal point are calculated. These vectors are set equal to the direction cosines of the resulting refraction vector, T . Next, the angle of changed direction at the refraction, $\theta = \theta_2 - \theta_1$, is calculated by means of the following vector identity so as to match the specified refraction vector (see Fig. 5):

$$\theta = \arccos(\hat{I}_x \cdot \hat{T}_x + \hat{I}_y \cdot \hat{T}_y + \hat{I}_z \cdot \hat{T}_z). \quad (10)$$

Snell's law gives

$$\tan \theta_1 = \frac{\eta_2 \sin \theta}{\eta_1 - \eta_2 \cos \theta}, \quad (11)$$

and, finally, the modified normal vector is given by

$$N = \frac{T - \frac{\eta_2}{\eta_1} \cdot I}{\frac{\eta_2}{\eta_1} \cdot \cos \theta_1 + \sqrt{1 - \left(\frac{\eta_2}{\eta_1}\right)^2 \cdot (1 - \cos \theta_1)^2}}, \quad (12)$$

where η_1 and η_2 are the refractive indices of two media after and before the surface, respectively. I is the incoming ray vector with the same direction as the refracted ray vector calculated at the previous anterior IOL surface.

The coordinates, (x, y, z) , of the specified focal point are the same as those obtained for the minimum spot radius in the ray-tracing analysis with pupil diameter 3 mm [close to paraxial conditions; Fig. 4(b)]. Figure 6 shows the result of ray tracing through the entire optical system with the modified posterior IOL surface. The skew rays, particularly the peripheral ones, have been “straightened up” and the modified system produces an image of the point source free from aberrations at the specified focal point. The improved imaging quality is analyzed in the spot diagrams in Fig. 7. The distribution of rays is circular and symmetric on both sides of the focal point, and the RMS values of the spread are significantly lower than in the unmodified system (Fig. 4). The RMS values at the z position 1.00 mm from that of the minimum spot radius was reduced by approximately 50%; see Table 2. Since the modified systems produce an aberration-free image of the point source, the Strehl ratio takes the value 1.00. It should be noted that diffraction effects were not included in the ray-tracing model. The Strehl ratio of a diffraction-limited system is typically ~ 0.8 . Furthermore, Fig. 8 illustrates the deviation of the normal vector distribution of the modified posterior IOL surface from that of an ideal spherical surface with the same radius of curvature (-20.0 mm). The average directional change of the normal vectors amounts to 3.0° . The largest deviation, up to 8.0° , is found at the periphery of the IOL surface (particularly at the lower rim), whereas the central part exhibits significantly smaller deviations, in the range from 0° to about 5° . That is, the periphery rays of the optical system are responsible for significantly larger refraction errors than the central rays.

Table 2. Summary of Ray-Tracing Results, On-Axis System

	z (mm)	RMS r (mm)	Strehl Ratio	Centroid x (mm)	Centroid y (mm)
Pupil diameter 6 mm	20.77	0.1627	0.074 ^a	-0.0018	0.2511
	21.77	0.1387		0.0032	0.2593
	22.77	0.1624		0.0080	0.2674
Pupil diameter 3 mm	20.79	0.0826	0.218 ^a	-0.0261	0.1125
	21.79	0.0680		-0.0277	0.1182
	22.79	0.0829		-0.0292	0.1240
Pupil diameter 6 mm with modified IOL	20.77	0.0852	1.00 ^a	-0.0018	0.2511
	21.77	0.0000		0.0032	0.2593
	22.77	0.0852		0.0080	0.2674
Pupil diameter 3 mm with modified IOL	20.79	0.0473	1.00 ^a	-0.02609	0.11252
	21.79	0.0000		-0.02765	0.11825
	22.79	0.0473		-0.02921	0.12397

^aAverage value for the three x - y planes around the focus; Figs. 4 and 7.

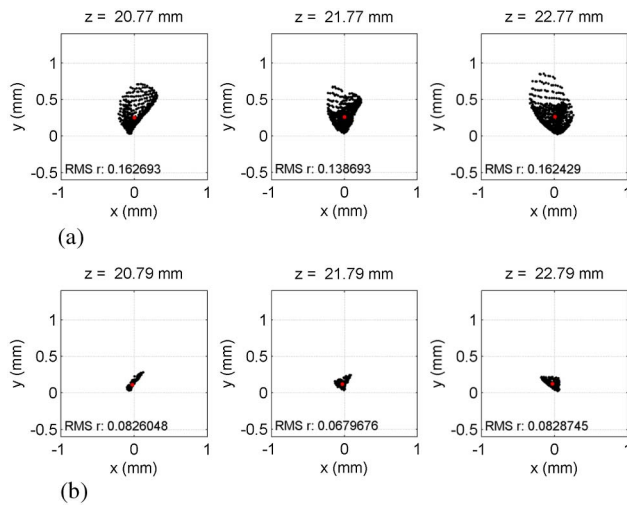


Fig. 4. Spot diagrams showing the intersections of rays with three consecutive x - y planes around the focal point at the position of the retina. The severe refractive errors result in aberrations and a blurred image of the point source. The red point in the center of each diagram indicates the centroid of the ray distribution. (a) A pupil diameter of 6 mm results in a minimum RMS value of the spread of 0.14 mm at $z = 21.77$ mm. (b) The same analysis as in (a), but with a pupil diameter of 3 mm, resulting in a minimum RMS value of the spread of 0.068 mm at $z = 21.79$ mm.

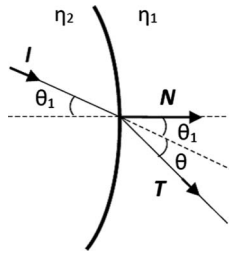


Fig. 5. Calculation of a modified normal vector, N , on the posterior IOL surface. η_1 and η_2 are the refractive indices of the vitreous chamber and that of the IOL, respectively. T is the specified direction of the refraction vector. The angle of changed direction θ at the refraction is calculated by means of the vector identity given in Eq. (11). θ_1 and N are calculated by means of Eqs. (11) and (12), respectively.

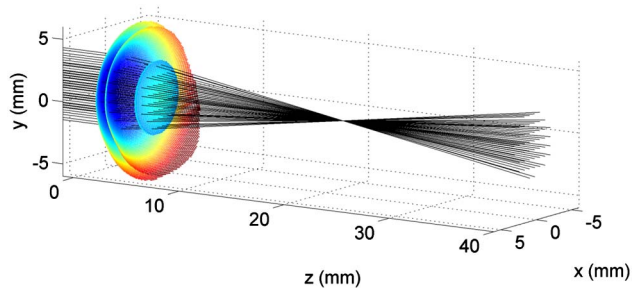


Fig. 6. Ray tracing through the same optical system as in Fig. 3, but with a modified lens posterior surface. The angles of the normal vectors of the surface are slightly modified to straighten up the rays. Pupil diameter is 6 mm, with an object point source object located at infinity (parallel incoming rays).

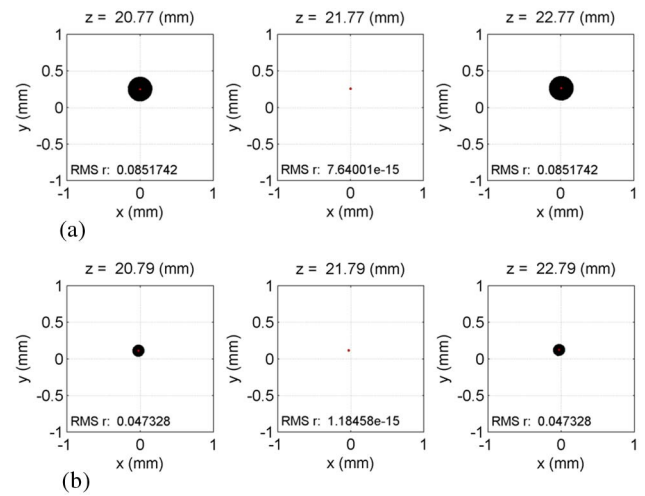


Fig. 7. Spot diagrams showing the improved imaging quality as a result of the modified posterior IOL surface. The red spots indicate the centroid of the ray distribution. (a) Pupil diameter 6 mm. (b) Pupil diameter 3 mm.

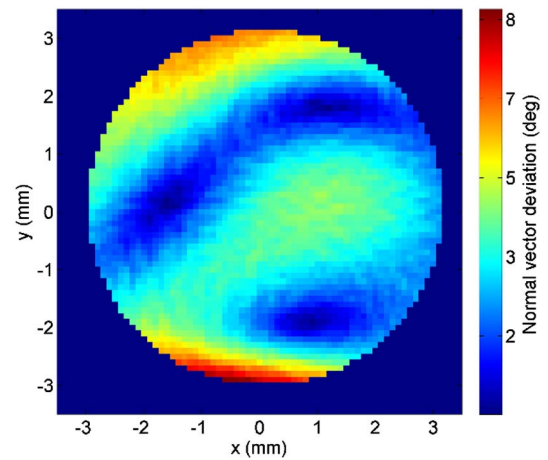


Fig. 8. Deviation of the normal vector distribution from that of an ideal spherical surface.

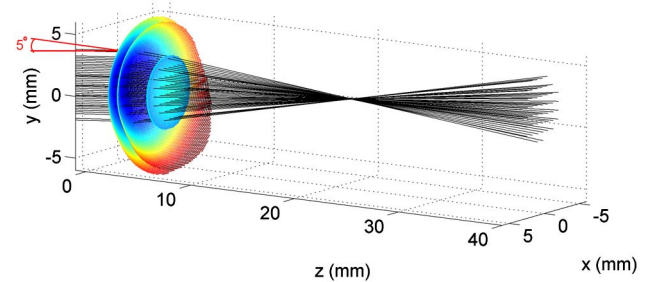


Fig. 9. 3D ray tracing through the same optical system as in Fig. 6, but with an off-axis angle of 5° . The modified normal vectors of the IOL posterior surface obtained from the on-axis system (Fig. 6) were used in the off-axis analysis. The pupil diameter is 6 mm, with an off-axis object point source object located at infinity (parallel incoming rays).

Table 3. Summary of Ray Tracing Results, Off-Axis System

	z (mm)	RMS r (mm)	Strehl ratio	Centroid x (mm)	Centroid y (mm)
Pupil diameter 6 mm	20.67	0.1629	0.065 ^a	1.2557	0.2505
	21.67	0.1388		1.3240	0.2587
	22.67	0.1628		1.3923	0.2670
Pupil diameter 6 mm with modified IOL	20.67	0.0875	0.148 ^a	1.2556	0.2444
	21.67	0.0242		1.3238	0.2523
	22.67	0.0905		1.3921	0.2602

^aAverage value for the three x - y planes around the focus; Fig. 10.

B. Off-Axis System

Object points located along the visual axis of the eye normally provide the best image quality at the fovea where the neural resolution is optimal. However, the imaging quality is also of importance for objects located slightly off axis. The fovea allows resolution of fine details in the central 5° of the visual field [23]. Therefore, we analyzed the imaging quality with the same optical system (the same corneal data, and the same IOL and ocular parameters) but with the object point source located at an angle of 5° relative to the visual axis. This was done in the simulation by setting the point source 5° off axis at infinity ($P_0 = (8749, 0, -100, 000)$ mm).

Figure 9 shows the visualization of the off-axis ray-tracing system, with the same modified IOL as in the on-axis system. Table 3 summarizes the results of the off-axis analysis. It can be seen that the image point at the retina is shifted ~1.3 mm along the x direction, which is almost the physical size of the fovea [26]. The resulting minimum RMS value [Fig. 10(a)] for the unmodified off-axis system (~0.139 mm) is the same as for the on-axis system. However, the modified off-axis system [Fig. 10(b)] resulted in a higher RMS value (~0.024 mm) at the minimum spot radius than that of the on-axis system, but this is, on the other hand, a significant improvement (reduction of ~83%) in comparison to the unmodified off-axis system. The RMS values at the z position 1.00 mm from that of the minimum spot radius were similar to those obtained in

the on-axis analysis, a reduction of ~50% with the modified IOL, as seen in Table 3.

5. DISCUSSION AND CONCLUSION

We propose a 3D ray-tracing model that can provide new possibilities for simulations and design of IOLs in order to compensate for the advanced refractive errors resulting from pathological deformed corneas, such as in KC. The model is based on measurement data (Scheimpflug photography) of the corneal anterior and posterior surfaces. A 3D version of Snell's law was implemented to calculate the refraction of rays. Intersection points and normal vectors of the measured surfaces were calculated by means of second-degree polynomial approximation of a number of surface elements. An ideal IOL was modeled by means of second-degree surfaces. Results of the 3D ray-tracing calculation with input corneal data from a patient with advanced KC were evaluated in terms of spot diagrams and RMS values on the retina, for on-axis and off-axis geometries, respectively. The imaging quality was low as a result of advanced refraction errors due to KC. Moreover, with the ray-tracing model as a basis, we presented an approach to modify the normal vectors of the IOL posterior surface. The modified normal vectors represented a free-form shape that can compensate for any type of advanced refractive error. Modified normal vectors of the posterior IOL surface were computed in the on-axis analysis, which led to a significant improvement of the imaging quality (RMS values reduced ~50% close to the retina). We also showed that off-axis rays (off-axis angle 5°), when introducing the same modified IOL, resulted in about the same improved quality as in the on-axis case.

Further studies should be undertaken to develop the present simulation method, to investigate the accuracy and resolution, and to conduct parameter studies with increasing numbers of rays. This also includes assessing the optimal number of grid points in relation to the number of parameters in Eq. (1) for the fitting procedure. Moreover, alternative methods to model the modified IOL surface, e.g., by means of Zernike sag polynomials, should be studied.

Experimentally, a phantom study, by using porcine eyes, for example, should be performed to confirm the simulations [27,28]. Another question to be addressed is new design of free-form customized IOLs. This concept study serves as a promising initial approach to the design of customized IOLs. Such a customized IOL would provide a perfect image on the retina. However, it should be mentioned that there might be some drawbacks with a customized IOL, such as tilt or decentration of the lens, that would decrease the quality of

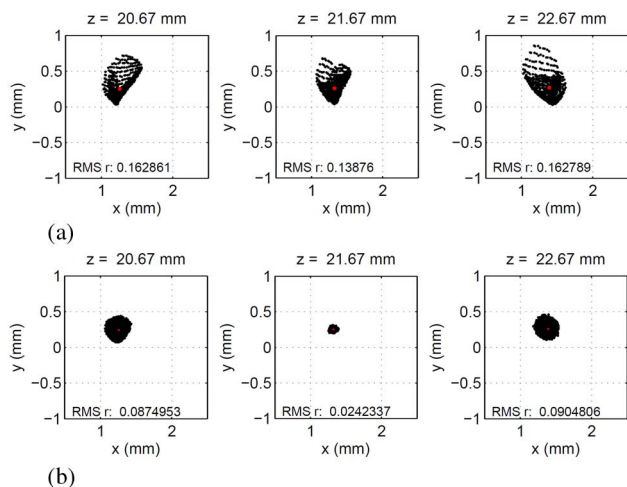


Fig. 10. Spot diagrams showing the imaging quality in the off-axis system. The minimum RMS values are found at $z = 21.67$ mm. Pupil diameter is 6 mm. (a) Ideal spherical posterior IOL surface. (b) Modified posterior IOL surface with the same set of modified normal vectors as calculated in the on-axis analysis.

the retinal image. This has also been pointed out in the literature; see e.g., Ref. [14]. On the other hand, the result of the off-axis analysis presented here indicates that a moderate tilt of the entire optical system ($\leq 5^\circ$) does not substantially decrease the imaging quality. In a first step to study misalignment of the optimized IOL, we performed a tolerance analysis with moderate decentrations in the vertical direction. The RMS values as a result of pure decentrations of 0.10 and 0.30 mm with a pupil diameter of 6 mm were found to be 0.011 and 0.022 mm, respectively, at the focal point ($z = 21.77$ mm). These values are significantly lower (92% and 84%) than in the case of the unmodified IOL (Table 2). This indicates that a small decentration of the IOL would only marginally reduce the visual acuity. To assess the combined effects of misalignment (decentration, tilt, and rotation), extensive tolerance analyses are needed. This will be a subject for future investigations.

Moreover, the presented 3D ray-tracing model can be used for analysis of refraction through any transparent smooth surface. It was found, in particular, that the model is suitable for analysis of refractive errors in KC. The eye model is applied to measurement data of the elevation of the cornea surfaces obtained by means of Scheimpflug photography, but structural raw data from other sources, such as optical coherence tomography, could also be used. Disorders that, like KC, affect the geometrical shape of the cornea drastically degrade vision quality. The present 3D ray-tracing model can constitute a basis for simulation of specially designed IOLs that are able to correct the advanced, irregular refractive errors in KC.

Funding. “Stiftelsen Kronprinsessan Margaretas Arbetsnämnd för synskadade”, Sweden.

REFERENCES

1. J. H. Krachmer, R. S. Feder, and M. W. Belin, “Keratoconus and related noninflammatory corneal thinning disorders,” *Surv. Ophthalmol.* **28**, 293–322 (1984).
2. D. T. Tan and Y. M. Por, “Current treatment options for corneal ectasia,” *Curr. Opin. Ophthalmol.* **18**, 284–289 (2007).
3. G. Wollensak, E. Spoerl, and T. Seiler, “Riboflavin/ultraviolet-A-induced collagen crosslinking for the treatment of keratoconus,” *Am. J. Ophthalmol.* **135**, 620–627 (2003).
4. A. Behndig, P. Montan, U. Stenevi, M. Kugelberg, C. Zetterstrom, and M. Lundstrom, “Aiming for emmetropia after cataract surgery: Swedish National Cataract Register study,” *J. Cataract Refract. Surg.* **38**, 1181–1186 (2012).
5. A. Behndig, P. Montan, U. Stenevi, M. Kugelberg, and M. Lundstrom, “One million cataract surgeries: Swedish National Cataract Register 1992–2009,” *J. Cataract Refract. Surg.* **37**, 1539–1545 (2011).
6. M. Lundstrom, A. Behndig, M. Kugelberg, P. Montan, U. Stenevi, and W. Thorburn, “Decreasing rate of capsule complications in cataract surgery: eight-year study of incidence, risk factors, and data validity by the Swedish National Cataract Register,” *J. Cataract Refract. Surg.* **37**, 1762–1767 (2011).
7. M. Claesson and W. J. Armitage, “Clinical outcome of repeat penetrating keratoplasty,” *Cornea* **32**, 1026–1030 (2013).
8. G. R. Mello, C. J. Roberts, D. Smadja, C. C. Serpe, R. R. Krueger, and M. R. Santhiago, “Comparison of keratometric changes after myopic ablation: ray tracing versus simulated keratometry,” *J. Refract. Surg.* **29**, 604–610 (2013).
9. G. Savini, A. Calossi, M. Camellin, F. Carones, M. Fantozzi, and K. J. Hoffer, “Corneal ray tracing versus simulated keratometry for estimating corneal power changes after excimer laser surgery,” *J. Cataract Refract. Surg.* **40**, 1109–1115 (2014).
10. L. Wang, A. M. Mahmoud, B. L. Anderson, D. D. Koch, and C. J. Roberts, “Total corneal power estimation: ray tracing method versus Gaussian optics formula,” *Invest. Ophthalmol. Vis. Sci.* **52**, 1716–1722 (2011).
11. H. Guo, A. V. Goncharov, and C. Dainty, “Comparison of retinal image quality with spherical and customized aspheric intraocular lenses,” *Biomed. Opt. Express* **3**, 681–691 (2012).
12. P. Rosales and S. Marcos, “Customized computer models of eyes with intraocular lenses,” *Opt. Express* **15**, 2204–2218 (2007).
13. J. Einighammer, T. Oltrup, T. Bende, and B. Jean, “The individual virtual eye: a computer model for advanced intraocular lens calculation,” *J. Optom.* **2**, 70–82 (2009).
14. J. Einighammer, T. Oltrup, E. Feudner, T. Bende, and B. Jean, “Customized aspheric intralocular lenses calculated with real ray tracing,” *J. Cataract Refract. Surg.* **35**, 1984–1994 (2009).
15. A. Sharma and A. K. Ghatak, “Ray tracing in gradient-index lenses—computation of ray-surface intersection,” *Appl. Opt.* **25**, 3409–3412 (1986).
16. G. H. Spencer and M. V. R. Murty, “General ray-tracing procedure,” *J. Opt. Soc. Am.* **52**, 672–678 (1962).
17. S. Ortiz, D. Siedlecki, L. Remon, and S. Marcos, “Three-dimensional ray tracing on Delaunay-based reconstructed surfaces,” *Appl. Opt.* **48**, 3886–3893 (2009).
18. A. S. Glassner, *An Introduction to Ray Tracing* (Academic, 1989).
19. T. B. Andersen, “Evaluating rms spot radii by ray tracing,” *Appl. Opt.* **21**, 1241–1248 (1982).
20. A. Jannings, “Sphere fit (least squared),” (2013), <http://www.mathworks.com/matlabcentral/fileexchange/34129-sphere-fit-least-squared>.
21. R. Navarro, J. Santamaria, and J. Bescos, “Accommodation-dependent model of the human-eye with aspherics,” *J. Opt. Soc. Am. A* **2**, 1273–1281 (1985).
22. S. Barbero, S. Marcos, J. Montejo, and C. Dorronsoro, “Design of isoplanatic aspheric monofocal intraocular lenses,” *Opt. Express* **19**, 6215–6230 (2011).
23. M. Bass, C. DeCusatis, J. Enoch, V. Lakshminarayanan, G. Li, C. MacDonald, V. Mahajan, and E. Van Stryland, *Handbook of Optics*, 3rd ed., Vol. III of Vision and Vision Optics (McGraw-Hill, 2009).
24. F. L. Pedrotti and L. S. Pedrotti, “Aberration theory,” in *Introduction to Optics*, 2nd ed. (Prentice-Hall, 1993), pp. 93–96.
25. L. N. Thibos, X. Hong, A. Bradley, and R. A. Applegate, “Accuracy and precision of objective refraction from wavefront aberrations,” *J. Vis.* **4**, 329–351 (2004).
26. R. V. Krstic, *Human Microscopic Anatomy: An Atlas for Students of Medicine and Biology* (Springer, 1991).
27. M. Zhao, A. N. Kuo, and J. A. Izatt, “3D refraction correction and extraction of clinical parameters from spectral domain optical coherence tomography of the cornea,” *Opt. Express* **18**, 8923–8936 (2010).
28. A. N. Kuo, R. P. McNabb, M. Zhao, F. LaRocca, S. S. Stinnett, S. Farsiu, and J. A. Izatt, “Corneal biometry from volumetric SDOCT and comparison with existing clinical modalities,” *Biomed. Opt. Express* **3**, 1279–1290 (2012).